High-field $^{57}Fe$ Mössbauer spectrometry study of the iron spin structure in Fe-R-B (R = Ho, Dy) amorphous ribbons



1998 J. Phys.: Condens. Matter 10 7065

(http://iopscience.iop.org/0953-8984/10/31/022)

J. Phys.: Condens. Matter **10** (1998) 7065–7078. Printed in the UK PII: S0953-8984(98)91643-5

# High-field $^{57}$Fe Mössbauer spectrometry study of the iron spin structure in Fe–R–B (R = Ho, Dy) amorphous ribbons

G Ravach and J Teillet†

GMP, Magnétisme et Applications, UMR CNRS 6634, Université de Rouen, F-76821 Mont-Saint-Aignan Cédex, France

Received 13 February 1998

**Abstract.** The magnetic structure of the iron in melt-spun amorphous ribbons with the compositions $Fe_{64}Ho_{16}B_{20}$ and $Fe_{66}Dy_{14}B_{20}$ was investigated using high-field $^{57}$Fe Mössbauer spectrometry. The low-temperature ($T \leqslant 10$ K) variation of the hyperfine parameters under fields ranging from 0 to 8 T is reported. A geometrical model was developed that accounts quantitatively for the experimental results. It describes the evolution of the spin structure in the framework of angular deformation of the cone formed by the iron magnetic moments. It is shown that $Fe_{64}Ho_{16}B_{20}$ exhibits a collinear spin structure of the iron from 2 T, while in $Fe_{66}Dy_{14}B_{20}$, the iron spins remain distributed at random within a cone up to 8 T. At 8 T, the semi-angle of the cone apex amounts to about 73°.

## 1. Introduction

Amorphous alloys based on transition metal (TM) and rare-earth (R) elements attract a lot of attention due to their interesting magnetic properties [1]. They combine strong magnetizations and high Curie temperatures, due to the transition metal, with strong anisotropy, owing to the presence of the rare earth. In addition to the possibility that they offer to study 3d–4f magnetism for a continuous range of the rare-earth concentration, these alloys can also exhibit random magnetic anisotropy [2, 3]. The distribution of the local easy-magnetization axes over the various atomic sites arises from the combination of the topological disorder, which induces a distribution of atomic environments within the alloy, and the spin–orbit coupling, which is generally strong for rare-earth elements [4–6]. In such alloys, magnetic structures result from the competition between exchange interactions, that tend to induce collinear spin structures, and random anisotropy, that spreads the moment directions in space. As a consequence, depending on the nature and the concentration of the transition metal and the rare-earth elements, a large variety of magnetic structures can be achieved. For instance, a collinear ferrimagnetic order is observed in a-$GdCo_3$ [7], while non-collinearity of the rare-earth sublattice is found in a-$NdCo_3$ [3] and a-$DyCo_3$ [8]. In a-$NdFe_3$ [3] and a-$TbFe_2$ [9, 10], both the iron and rare-earth sublattices are non-collinear.

These magnetic structures can also be investigated in ternary amorphous TM–R–Me alloys, where Me is a metalloid element. These systems are easily produced in the form of ribbons by the usual melt-spinning technique. In particular, alloys with compositions such as $TM_{80-x}R_xMe_{20}$ allow the study of ranges of low rare-earth concentration. Over the last decade, magnetization studies dedicated to alloys with $x \leqslant 16$ at.%, typically, have

† Author to whom any correspondence should be addressed; e-mail: jacques.teillet@univ-rouen.fr.

0953-8984/98/317065+14$19.50  

been quite numerous [11–24], and conical spin structures in the rare-earth sublattice were deduced for some of these alloys. The average semi-angles of the cone apex were estimated to be 40° for Co–Er–B [11], Fe–Dy–B [25] and Fe–Tm–B–Si [23], 100° for Fe–Nd–B and Fe–Sm–B [22] and 54° for Fe–Er–B–Si [14]. Collinear rare-earth magnetic structures were found in Co–Gd–B [13], Co–Ho–B [15] and Fe–Ho–B [18].

One needs to formulate some hypotheses about the transition metal spin structure to extract information on the rare-earth spin structure from magnetization measurements. In particular, in the previous studies, it was assumed, first, that the TM spin structure does not change with the rare-earth concentration and, second, that it is collinear. As a consequence, any variation in the TM mean magnetic moment with the rare-earth content was attributed to 3d–5d hybridization effects. For Fe-based alloys, using high-field $^{57}$Fe Mössbauer spectrometry measurements, it is possible to gain access to the iron sublattice, irrespective of any knowledge of the rare-earth magnetic behaviour. In fact, such studies showed that the iron spin structure is collinear in $Fe_{80-x}Er_xB_{20}$ ($x \leqslant 4$ at.%) and $Fe_{72}Er_8B_{12}Si_8$ [12, 26], while some departure from collinearity was found in $Fe_{65}Er_{15}B_{12}Si_8$ [14]. From a fundamental point of view, it is thus of most interest to perform such high-field Mössbauer studies on Fe-based amorphous ribbons containing various rare earths, and the present paper deals with the results obtained in the cases of $Fe_{64}R_{16}B_{20}$ (R = Ho, Dy) alloys. A model was developed to account for our experimental data. It allows us to describe quantitatively the evolution of the iron spin structure under increasing applied magnetic field.

## 2. Experimental procedure

Ingots of alloys of nominal compositions $Fe_{64}R_{16}B_{20}$ (R = Ho, Dy) were prepared by induction melting from elements of purity higher than 99.9% (99.99% in the case of the iron). The melting was performed under an inert atmosphere of argon to prevent the rare-earth element from oxidizing. In order to limit the preferential rare-earth evaporation generally observed during melting [20], we proceeded in two steps. The first stage consisted in producing the corresponding Fe–B alloy. As its composition is close to the deep eutectic in the Fe–B binary phase diagram [27], its melting point (about 1520 K) is strongly decreased compared with those of pure iron and boron (respectively 1809 K and 2350 K). This first step facilitates the melting of the rare-earth element when it is added to Fe–B, and reduces its tendency to evaporate. Ribbons were then obtained from the ingot by the usual melt-spinning technique, under an argon flow. The ejection of the melt alloy was performed on a copper wheel with a tangential velocity of 35 m s$^{-1}$ under a helium pressure of $4 \times 10^4$ Pa. The compositions of the ribbons were determined by electron probe microanalysis, with 1 at.% accuracy. The rare-earth contents were estimated to be 16 at.% (Ho) and 14 at.% (Dy). We verified that the as-quenched ribbons were amorphous by means of room temperature x-ray diffraction using Co K$\alpha_1$ radiation and $^{57}$Fe transmission Mössbauer spectrometry [28].

Mössbauer samples made of parallel ribbons were set in a plane perpendicular to the $\gamma$-beam direction. The Mössbauer experiments were performed under external magnetic fields $B_a$ ranging from 0 to 8 T and applied along the $\gamma$-beam direction, i.e. perpendicularly to the ribbon plane. The Mössbauer spectra were recorded over the 4.2–10 K temperature range using a source of $^{57}$Co embedded in a rhodium matrix. The spectra were computer fitted by a least-squares technique [29], using the histogram method relative to discrete distributions of single crystals [30], and constraining the linewidth of each elementary sextet to be the same. Because of the topological disorder, we assumed the mean quadrupolar shift to be zero. Let us recall that the relative intensities of the sextet lines depend on the mean angle $\beta$ between the incident $\gamma$-beam direction and the hyperfine fields ($\boldsymbol{B}_{hf}$), or effective fields

($\boldsymbol{B}_{eff}$) in the case of applied-field experiments. The ratios of the lines vary as 3:$y$:1:1:$y$:3 with $y$ expressed as

$$y = \frac{4\sin^2\beta}{1+\cos^2\beta}.$$

For instance, a random distribution of hyperfine-field directions over the whole space would lead to $y = 2$, i.e. $\beta = 54.7^\circ$. Owing to our choice of experimental configuration, the Mössbauer angle $\beta$ gives the mean orientation of the effective fields $\boldsymbol{B}_{eff}$ relatively to the external magnetic field $\boldsymbol{B}_a$, when one is applied.

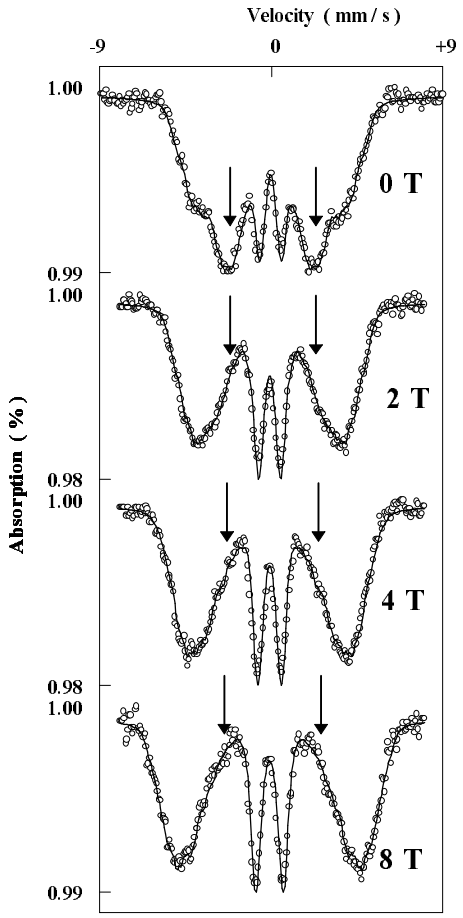


**Figure 1.** $Fe_{64}Ho_{16}B_{20}$ Mössbauer spectra at 10 K as functions of the external magnetic field $B_a$. The continuous lines are computer fittings to the data. Arrows indicate the positions of $\Delta m = 0$ lines.

## 3. Experimental results

### *3.1. Mössbauer spectra*

All of the Mössbauer spectra exhibit broadened lines, typical of a distribution of iron environments within the ribbons (see figure 1 and figure 2). Some overlapping between the lines is observed in most of the spectra. On increasing the magnetic field $B_a$, the intermediate lines of the $Fe_{64}Ho_{16}B_{20}$ spectra progressively lessen in intensity, until they completely vanish between 2 and 4 T (see figure 1), indicating a progressive rotation of

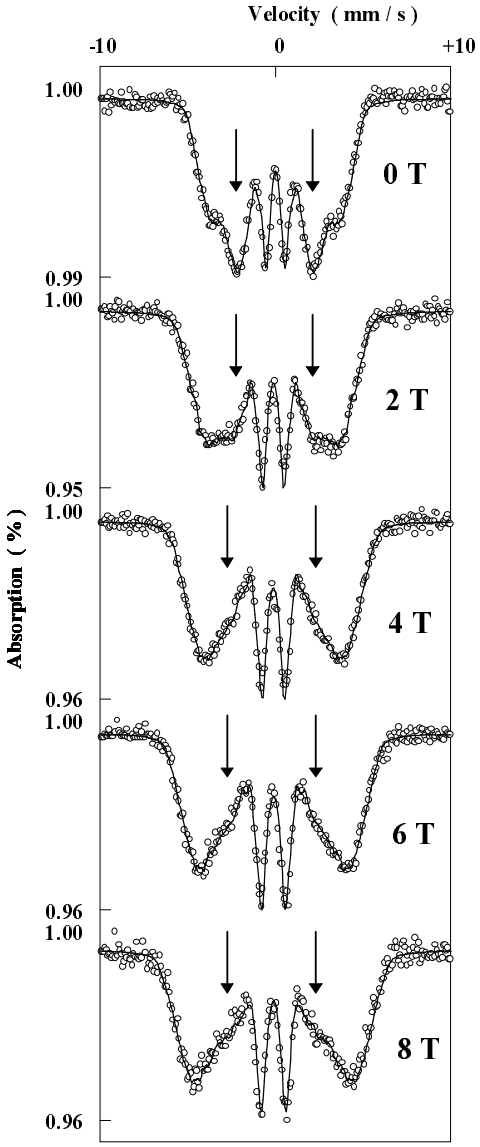


**Figure 2.** $Fe_{66}Dy_{14}B_{20}$ Mössbauer spectra at 4.2 K as functions of the external magnetic field $B_a$. The continuous lines are computer fittings to the data. Arrows indicate the positions of $\Delta m = 0$ lines.

the hyperfine fields $\boldsymbol{B}_{hf}$ towards the applied-field direction. For higher fields, no further significant evolution of the relative intensities of the lines is detected, suggesting that complete alignment was achieved. A lessening of the intensity of the intermediate lines with increasing magnetic field is also observed for $Fe_{66}Dy_{14}B_{20}$ Mössbauer spectra, but the maximum available field (8 T) does not cause them to completely vanish (figure 2). The lessening in intensity of the intermediate lines does not continue above 4 T, indicating that after a partial rotation, the hyperfine fields become frozen in a configuration which is not collinear with $\boldsymbol{B}_a$.

**Table 1.** Mean hyperfine parameters deduced from the fits of the ribbon spectra of $Fe_{64}Ho_{16}B_{20}$ and $Fe_{66}Dy_{14}B_{20}$ as functions of the applied field $B_a$. The values given in parentheses correspond to the errors as deduced from the fits.

| Alloy | $B_a$ (T) | $\langle B_{eff} \rangle$ (T) | $\beta$ (deg) |
|---|---|---|---|
| $Fe_{64}Ho_{16}B_{20}$ | 0 | 19.7 (2) | 52 (5) |
| (10 K) | 2 | 21.5 (2) | 17 (10) |
| | 4 | 23.7 (2) | 12 (10) |
| | 8 | 27.8 (2) | 0 (15) |
| $Fe_{66}Dy_{14}B_{20}$ | 0 | 20.1 (2) | 53 (5) |
| (4.2 K) | 2 | 21.6 (2) | 46 (5) |
| | 4 | 23.2 (2) | 39 (5) |
| | 6 | 24.6 (2) | 37 (5) |
| | 8 | 26.2 (2) | 35 (5) |

### *3.2. Mean hyperfine parameters*

The mean values of the effective field $\langle B_{eff} \rangle$ and the Mössbauer angle $\beta$ are reported in table 1 for both alloys. For $Fe_{64}Ho_{16}B_{20}$, $\beta$ rapidly decreases as $B_a$ increases. Taking into account the accuracy of the experimental values, $\beta$ is close to $0^\circ$ for $B_a \approx 4$ T. For $Fe_{66}Dy_{14}B_{20}$ alloy, the decrease of $\beta$ is very weak and reaches saturation with $\beta$ close to $35^\circ$. For both alloys, the variation of $\beta$ is compatible with the evolution of the relative intensities of the lines of the Mössbauer spectra.

The effective field $\boldsymbol{B}_{eff}$ acting on a given iron-atom site is defined as

$$\boldsymbol{B}_{eff} = \boldsymbol{B}_{hf} + \boldsymbol{B}'_a$$

with

$$\boldsymbol{B}'_a = \boldsymbol{B}_a + \boldsymbol{B}_d + \boldsymbol{B}_L + \boldsymbol{B}_{dip}$$

where $\boldsymbol{B}_d$ is the demagnetizing field, $\boldsymbol{B}_L$ is the Lorentz field and $\boldsymbol{B}_{dip}$ accounts for the contributions of the external dipoles within the Lorentz sphere. In random systems, the dipole sum usually vanishes, and $\boldsymbol{B}_{dip}$ will not be taken into consideration in our analysis.

No demagnetizing-field data are available for our alloys; thus $B_d$ was roughly estimated from the saturation magnetizations $\sigma_s$, assuming that the demagnetizing factor is $N_z = 1$ for the normal to the plane of the ribbons. Magnetization measurements give $\sigma_s = 36.1$ A m$^2$ kg$^{-1}$ for a-$Fe_{66}Ho_{16}B_{18}$ at 6 K [18], and $\sigma_s = 14.8$ A m$^2$ kg$^{-1}$ for a-$Fe_{65.8}Dy_{14.2}B_{20}$ at 1.5 K [25]. As no precise density measurements have been performed up to now, we assumed a $\rho$-value of 7.55 g cm$^{-3}$, taken from the interpretation of anomalous wide-angle x-ray scattering experiments on amorphous Co–Er–B ribbons [31–33]. On the basis of this $\rho$-value, the demagnetizing fields amount to $B_d = 0.35$ T ($Fe_{64}Ho_{16}B_{20}$) and $B_d = 0.14$ T ($Fe_{66}Dy_{14}B_{20}$). With our assumption about the demagnetizing factor, the Lorentz fields $\boldsymbol{B}_L$ amount to a third of the demagnetizing fields. The values of $\boldsymbol{B}_d$ and $\boldsymbol{B}_L$ are low compared with the various other fields involved in our experiments, and their effect will be neglected in the following.

The hyperfine field $\boldsymbol{B}_{hf}$ is directed oppositely to the iron-atom moment $\boldsymbol{\mu}_{\mathrm{Fe}}$ [34]. Because of the ferrimagnetic coupling between the transition metals and the heavy rare earths, the Dy and Ho magnetizations are directed parallel to the iron hyperfine field $\boldsymbol{B}_{hf}$. In both alloys, the applied-field increase induces an enhancement of the mean effective field $\langle B_{eff} \rangle$ (table 1), indicating that the rare-earth magnetization dominates, in agreement with the compensation concentrations deduced from magnetization measurements

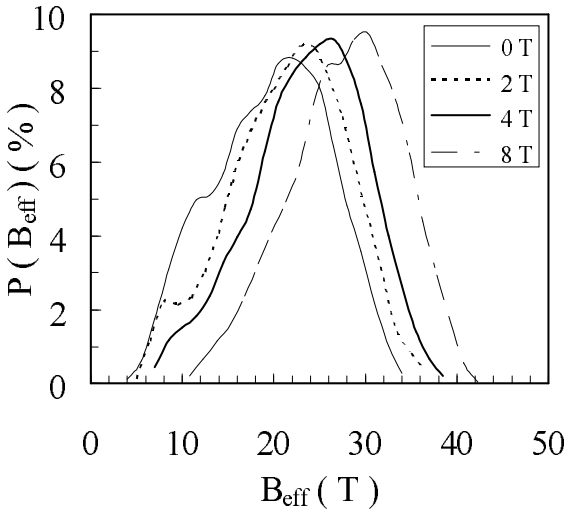


**Figure 3.** $Fe_{64}Ho_{16}B_{20}$ alloy (at 10 K): effective-field distributions as functions of the applied field $B_a$.

for $Fe_{82-x}Ho_xB_{18}$ ($x_{comp} = 13$ at.% at 6 K [18]) and for $Fe_{80-x}Dy_xB_{20}$ ($x_{comp} = 11.7$ at.% at 1.5 K [25]).

### *3.3. Effective-field distributions*

The effective-field distributions deduced from the fits are displayed in figure 3 (for $Fe_{64}Ho_{16}B_{20}$) and figure 4 (for $Fe_{66}Dy_{14}B_{20}$). Although discrete, these distributions are plotted as continuous or dashed lines in order to facilitate comparison.

*3.3.1. Zero-field experiments.* In the absence of an external magnetic field, the hyperfine-field distributions exhibit an intense broad peak at around 20 T and a prepeak at lower $B_{hf}$-values (centred at about 10 T). The physical meaning of the prepeak observed on the low-field side of the distribution is controversial. It was shown for some metallic glasses that such a prepeak could be due to an erroneous estimation of the magnetic texture, which is characterized by the Mössbauer angle $\beta$ [30]. In our spectra, such difficulties might arise from the overlapping that we observe between the lines. Mössbauer measurements were thus performed for a configuration which allows the collapse of magnetic texture effects (the so-called magic-angle configuration), so that the hyperfine-field distributions could be extracted unambiguously [35]. As we did not observe any difference in the results whatever configuration we chose (perpendicular or at the magic angle), the prepeak cannot be attributed to such effects. In fact, its presence is probably due to local quadrupolar effects that were not accounted for in our analysis, and which may lead to a deformation of the Mössbauer spectra. In fact, our analysis remains valid as long as the quadrupolar effects can be treated as a perturbation of the magnetic interaction [36]. For our alloys, the validity range corresponds approximately to $B_{hf}$-values above 11 T, which excludes the low-field contributions, and may explain the deformation of our distributions.

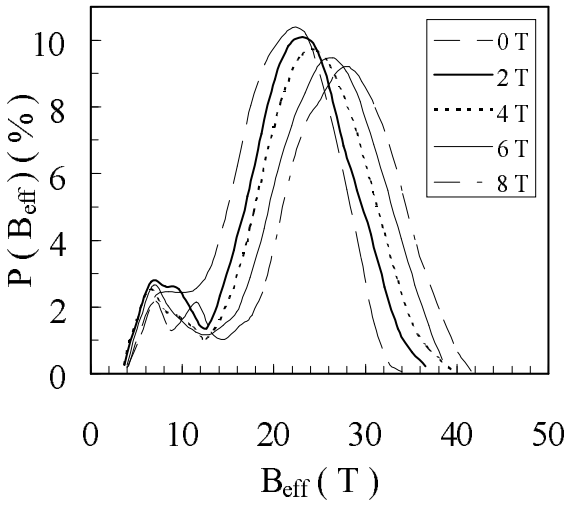


**Figure 4.** $Fe_{66}Dy_{14}B_{20}$ alloy (at 4.2 K): effective-field distributions as functions of the applied field $B_a$.

*3.3.2. The effect of the external field.* For $Fe_{64}Ho_{16}B_{20}$, the increase of $B_a$ induces a shift $\delta B_{eff}$ of the main peak of the effective-field distribution towards high-field values (figure 3). In agreement with previous observations, $\delta B_{eff}$ amounts to the variation $\delta B_a$ of the applied field. This behaviour is also observed for the variation of the mean effective field $\langle B_{eff} \rangle$ with $B_a$ (table 1). Between 0 and 2 T, the position of the prepeak does not vary significantly, while, above 2 T, these contributions also shift towards higher-field values. This evolution of the $B_{eff}$-distributions suggests an inhomogeneous deformation of the iron magnetic structure. High hyperfine fields rapidly orientate parallel to $\boldsymbol{B}_a$, complete alignment being realized from 2 T. As long as the applied field has not reached 2 T, low-hyperfine-field contributions are not collinear with $\boldsymbol{B}_a$. This behaviour might be due to strong random-anisotropy effects, freezing the iron magnetic moments, in rare-earth-rich zones. Above 2 T, those fields become aligned along $\boldsymbol{B}_a$, and complete alignment of all of the hyperfine fields along $\boldsymbol{B}_a$ is achieved between 2 and 4 T, in agreement with the evolution of the lines of the spectra (figure 1).

A shift of the main peak of the $B_{eff}$-distributions is also observed for $Fe_{66}Dy_{14}B_{20}$ alloy, but it corresponds to $\delta B_{eff} = 0.75\,\delta B_a$, in agreement with the freezing of the iron magnetic structure in a configuration which is not collinear with $\boldsymbol{B}_a$. The position of the prepeak only varies slightly under the application of the external field. Beyond 2 T, it tends to shift towards low-field values, while, above 2 T, it progressively shifts towards high fields. Contrary to the case for $Fe_{64}Ho_{16}B_{20}$ alloy, the maximum available field (8 T) is not high enough to cause the low hyperfine fields to align along $\boldsymbol{B}_a$.

## 4. Quantitative analysis of the iron magnetic structure

In order to describe quantitatively the evolution of the iron magnetic structure under an external field, we developed a simple geometric model with the aim of correlating the variations of the Mössbauer angle $\beta$ and the mean effective field $\langle B_{eff} \rangle$.

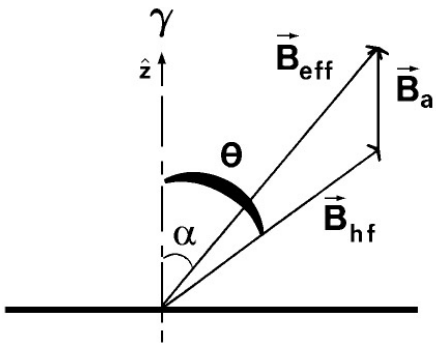


**Figure 5.** The applied field $\boldsymbol{B}_a$, hyperfine field $\boldsymbol{B}_{hf}$ and effective field $\boldsymbol{B}_{eff}$ at an iron-atom site.

### *4.1. Description of the model*

*4.1.1. Calculation of the mean effective field.* For a given iron atom, the intensity $B_{eff}$ of the effective field $\boldsymbol{B}_{eff}$ acting on the site is given by

$$B_{eff} = (B_{hf}^2 + B_a^2 + 2B_a B_{hf}\cos\theta)^{1/2}$$

where $\theta = (\boldsymbol{B}_a, \boldsymbol{B}_{hf})$ (figure 5).

The calculation of $\langle B_{eff}\rangle$ requires knowledge of the hyperfine-field distribution—as regards both modulus and direction—and we made the following assumptions.

(1) The distributions of the hyperfine-field modulus ($B_{hf}$) and direction (defined by the angle $\theta$) are independent. This hypothesis is usually made, and has been used for the fits of the zero-field spectra.

(2) For the modulus, we can use the hyperfine-field distribution deduced from the fit of the zero-field spectrum. Let us recall that this distribution is discrete and that, if $N_S$ is the number of sextets involved, it is defined by

$$P(B_{hf}) = P_i \qquad \text{if } B_{hf} = B_{hf}^i, \text{ for } i = 1, 2, \ldots, N_S.$$

We have implicitly assumed here the absence of induced moment effects under the application of the external field. This hypothesis thus corresponds to a description of the evolution of the iron spin structure in terms of angular deformation.

(3) Because of the topological disorder, the hyperfine-field directions are distributed within a cone which has an apex semi-angle $\theta_m$, and is centred around a $\hat{z}$-axis corresponding to the direction of the applied field $\boldsymbol{B}_a$. Furthermore, we considered the simple case of an equiprobable continuous repartition of those directions (and thus of the $\theta$-values). The latter assumption seems all the more reliable, as, for $B_a = 0$, the $\beta$-values are close to 54.7° (table 1), which is typical for $\boldsymbol{B}_{hf}$-directions distributed at random over the whole space.

According to these hypotheses, the mean effective field $\langle B_{eff}\rangle$ is given by

$$\langle B_{eff}\rangle = \left(\sum_{i=1}^{N_S} P_i \int_0^{\theta_m} B_{eff}^i \, \mathrm{d}\omega\right) \Big/ \left(\int_0^{\theta_m} \mathrm{d}\omega\right)$$

where $\mathrm{d}\omega = 2\pi \sin\theta \, \mathrm{d}\theta$, owing to the symmetry of the revolution around the $\hat{z}$-axis. As the calculation is not difficult we will not describe it in detail; we finally obtain

$$\langle B_{eff}\rangle = \frac{1}{3B_a(1-\cos\theta_m)} \sum_{i=1}^{N_S} \frac{P_i}{B_{hf}^i} C_i$$

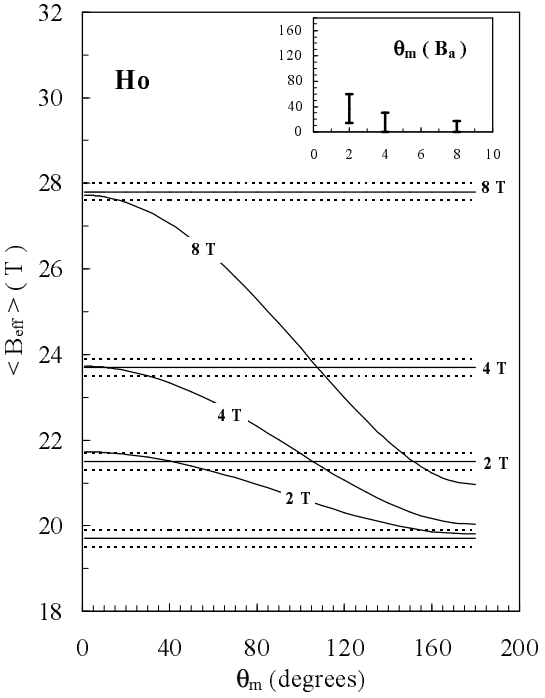


**Figure 6.** $Fe_{64}Ho_{16}B_{20}$ alloy: the variation of the mean effective field $\langle B_{eff}\rangle$ as a function of the iron cone semi-angle $\theta_m$ for the various experimental applied fields. The horizontal lines correspond to the experimental data for $\langle B_{eff}\rangle$, and the horizontal dashed lines delimit the uncertainty range. The inset corresponds to the values of $\theta_m$ which are compatible with both the model and the $\langle B_{eff}\rangle$ experimental data.

with

$$C_i = (B_a + B_{hf}^i)^3 - a_i^{3/2}$$
$$a_i = B_a^2 + (B_{hf}^i)^2 + 2B_a B_{hf}^i \cos\theta_m.$$

Using those relations, the variation of the mean effective field $\langle B_{eff}\rangle$ can be calculated as a function of the cone apex semi-angle $\theta_m$ for the various applied-field values $B_a$. From these curves, the $\theta_m$-values which are compatible with the experimental $\langle B_{eff}\rangle$ data can also be extracted.

*4.1.2. Calculation of the Mössbauer angle $\beta$.* The Mössbauer angle $\beta$ deduced from the fit of the spectra is defined as

$$\sin^2\beta = \langle \sin^2\alpha\rangle$$

where $\alpha$ represents the angle between the $\gamma$-beam direction (or the $\boldsymbol{B}_a$-direction) and the effective-field $\boldsymbol{B}_{eff}$-direction of one particular iron-atom site. From figure 5, it is seen that

$$\sin\alpha = \frac{B_{hf}}{B_{eff}}\sin\theta.$$

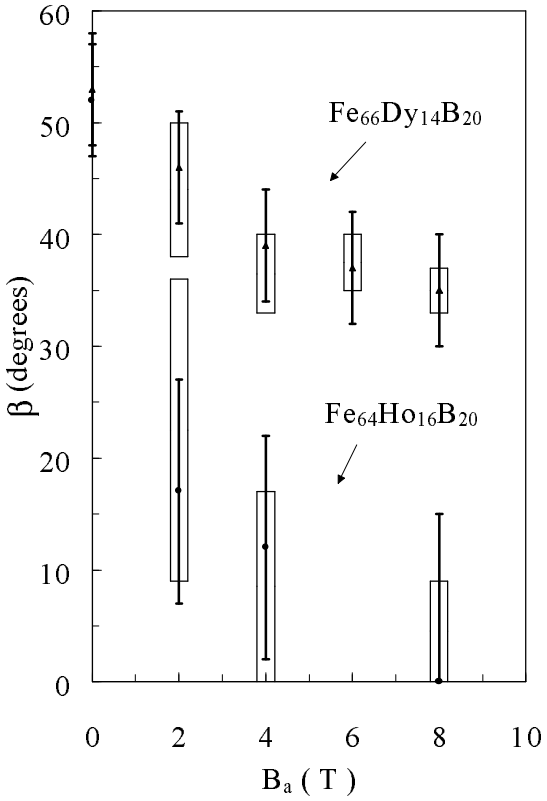


**Figure 7.** The Mössbauer angle $\beta$ as a function of the applied field for $Fe_{64}Ho_{16}B_{20}$ and $Fe_{66}Dy_{14}B_{20}$ alloys: calculated from the model for the $\theta_m$-values (open rectangles) and experimental data (black symbols).

Using hypotheses (1)–(3), $\sin^2\beta$ can thus be calculated as

$$\sin^2\beta = \frac{1}{8B_a^3(1-\cos\theta_m)}\sum_{i=1}^{N_S}\frac{P_i}{B_{hf}^i}(F_i+G_i)$$

where

$$F_i = -(B_a^2-(B_{hf}^i)^2)^2\ln\frac{(B_a+B_{hf}^i)^2}{a_i}$$

$$G_i = 2B_aB_{hf}^i(1-\cos\theta_m)\left[B_a^2+(B_{hf}^i)^2-B_aB_{hf}^i(1+\cos\theta_m)\right]$$

with the $a_i$ as defined previously.

### *4.2. Application of the model to the cases of $Fe_{64}Ho_{16}B_{20}$ and $Fe_{66}Dy_{14}B_{20}$ ribbons*

*4.2.1. $Fe_{64}Ho_{16}B_{20}$.* The curves for $\langle B_{eff}\rangle(\theta_m)$ deduced from the model are presented in figure 6 for $Fe_{64}Ho_{16}B_{20}$ alloy. They were calculated for the various applied-field values. In this figure, the continuous horizontal lines correspond to experimental data obtained for the mean effective field $\langle B_{eff}\rangle$. The ranges of possible $\theta_m$-values were determined, taking into account the accuracy deduced from the fits for $\langle B_{eff}\rangle$, which is delimited by dashed

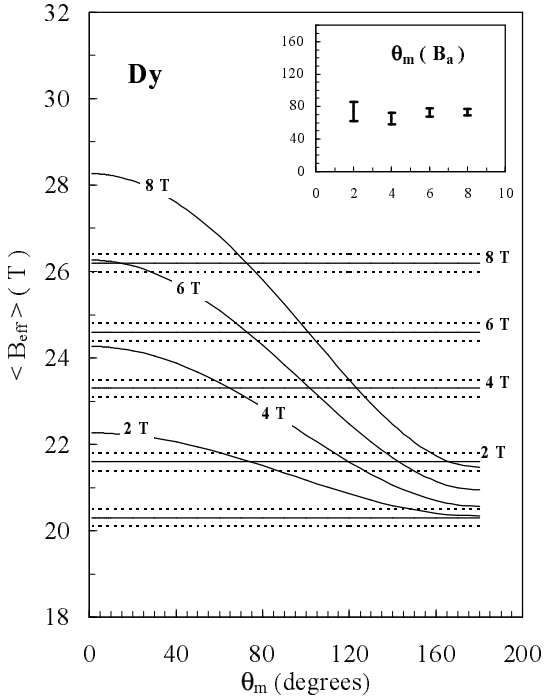


**Figure 8.** $Fe_{66}Dy_{14}B_{20}$ alloy: the variation of the mean effective field $\langle B_{eff}\rangle$ as a function of the iron cone semi-angle $\theta_m$ for the various experimental applied fields. The horizontal lines correspond to the experimental data for $\langle B_{eff}\rangle$, and the horizontal dashed lines delimit the uncertainty range. The inset corresponds to the values of $\theta_m$ which are compatible with both the model and the $\langle B_{eff}\rangle$ experimental data.

horizontal lines in figure 6. These ranges are presented in the inset of the figure. The results that we obtain confirm the rapid decrease of the iron-spin canting around $\boldsymbol{B}_a$. The values of the Mössbauer angle $\beta$ deduced from the model for these $\theta_m$-ranges are compared to the experimental data in figure 7. A very good agreement is observed, and the model quantitatively accounts for the variations of both the mean effective field $\langle B_{eff}\rangle$ and the Mössbauer angle $\beta$.

*4.2.2. $Fe_{66}Dy_{14}B_{20}$.* The results of the $\langle B_{eff}\rangle$ calculations are presented in figure 8 for $Fe_{66}Dy_{14}B_{20}$ alloy. The $\theta_m$-values which are compatible with the experimental mean effective fields are displayed in the inset in figure 8. They indicate a reduction of the canting of the iron spins between 0 and 2 T. At higher applied fields, we observe the expected saturation effect in the $\theta_m$-variation. The calculated Mössbauer angles reproduce perfectly the experimental data (figure 7) and the model also accounts for all of the results for this alloy.

### *4.3. Discussion*

For both alloys, a saturation effect is observed at around 2 T in the evolution of the iron cone with the applied field, in agreement with the saturation effect in the variation of the magnetization reported for $Fe_{82-x}Ho_xB_{18}$ [18] and $Fe_{80-x}Dy_xB_{20}$ [25]. Breaking of the

Fe–R ferrimagnetic coupling, which would induce an increase of the $\theta_m$-values, was not observed for any of our alloys.

When this saturation effect is reached, $Fe_{64}Ho_{16}B_{20}$ alloy exhibits collinear iron spin structure. Our results thus validate the hypothesis used for the interpretation of the magnetization measurements for $Fe_{82-x}Ho_xB_{18}$ alloys ($x \leqslant 16$ at.%), which concluded that the holmium sublattice is collinear [18]. The correlation of the latter and the present Mössbauer investigations thus shows that our $Fe_{64}Ho_{16}B_{20}$ ribbons are ferrimagnets (figure 9). Although spin–orbit coupling is strong in holmium, the random magnetic anisotropy due to holmium remains weak compared with exchange interactions, and the transition metal imposes its collinear magnetic structure on the rare-earth sublattice, via strong Fe–Ho exchange coupling.

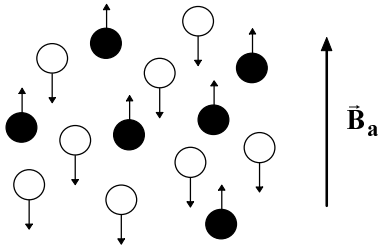


**Figure 9.** A schematic representation of the magnetic structure of ferrimagnetic $Fe_{64}Ho_{16}B_{20}$ alloy. Open (black) circles correspond to iron (holmium) atoms and arrows represent the magnetic moment directions.

In $Fe_{66}Dy_{14}B_{20}$, the iron magnetic moments are randomly distributed within a cone whose apex semi-angle $\theta_m$ still amounts to 69–77° at 8 T. This distribution of the iron moments within a cone is due to the strong random-anisotropy effect of the rare earth, which also leads to a non-collinear arrangement of the rare-earth moments [25]. In the latter study, only spreading of the rare-earth moments was considered to interpret the magnetization behaviour, and the Dy cone apex semi-angle was estimated to be 41.4°. Because of the manner in which it is calculated, this value is relative to the mean rare-earth cone. In order to compare the behaviours of the Fe and Dy sublattices, we calculated the mean value of $\theta$ for iron using

$$\langle\theta\rangle = \left(\int_0^{\theta_m} \theta \ \mathrm{d}\omega\right) \Big/ \left(\int_0^{\theta_m} \mathrm{d}\omega\right) = \frac{\sin\theta_m - \theta_m \cos\theta_m}{1 - \cos\theta_m}.$$

From this relation, the mean iron cone apex semi-angle is $\langle\theta\rangle = 45$–50°. This value indicates that the spreading of the moment directions is as important in the transition metal sublattice as in the rare-earth one. The dysprosium anisotropy thus induces a canting of the iron moments via the Fe–Dy exchange coupling, resulting in the sperimagnetic structure displayed in figure 10. From magnetization measurements, the iron mean magnetic moment can be estimated to be 1.64 $\mu_B$ for our alloy and extrapolation gave the value 1.95 $\mu_B$ for $Fe_{80}B_{20}$ [25]. The decrease of the iron moment was attributed to the effects of hybridization between 3d(Fe) and 5d(Dy) or sp(B) orbitals, assuming a collinear alignment of Fe moments. Our study shows that the spreading of the transition metal moment directions in space has to be accounted for to explain the variation of the iron magnetization. From our value of $\langle\theta\rangle$, the iron moment modulus can be estimated to be $1.96 \pm 0.04$ $\mu_B$ for our ribbons, and thus corresponds to the result obtained for $Fe_{80}B_{20}$. This would suggest that 3d–5d hybridization effects are much weaker in this composition range than previously thought.

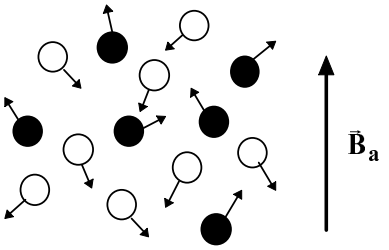


**Figure 10.** A schematic representation of the magnetic structure of sperimagnetic $Fe_{66}Dy_{14}B_{20}$ alloy. Open (black) circles correspond to iron (dysprosium) atoms and arrows represent the magnetic moment directions.

## 5. Conclusion

The iron spin structure of amorphous ribbons containing heavy rare-earth elements was investigated by high-field $^{57}$Fe Mössbauer spectrometry. We developed a geometrical model which accounts for the variations of both the mean effective field and its mean orientation relative to the applied-field direction. In this model, the iron moment directions are considered randomly distributed within cones. Their evolution under the applied field is described within the framework of angular deformation only, excluding induced-moment effects. The $Fe_{64}Ho_{16}B_{20}$ ribbons exhibit iron collinear spin structure from 2 T, showing that the random anisotropy of holmium is dominated by the effect of ferromagnetic Fe–Fe and ferrimagnetic Fe–Ho exchange interactions. In $Fe_{66}Dy_{14}B_{20}$ amorphous ribbons, iron magnetic moments remain randomly distributed within a cone with an apex semi-angle of about 73° up to 8 T. This spreading of the iron moments is as important as that deduced from magnetization measurements for the dysprosium sublattice. In this alloy, random anisotropy is induced by dysprosium in the transition metal sublattice, through Fe–Dy ferrimagnetic coupling. High-field Mössbauer studies are now in progress, in order to investigate the iron spin structure in ribbons containing light rare-earth elements.

## Acknowledgments

The authors would like to thank Dr R Krishnan, Dr H Lassri and Dr L Driouch from the Université de Versailles (France) for providing the samples. One of us (GR) is grateful to Dr J M Greneche for his hospitality and assistance with the high-field Mössbauer experiments partly performed at the Université du Maine (France), as well as for fruitful discussions.

## References

[1] Hansen P 1991 *Handbook of Magnetic Materials* vol 6, ed K H J Buschow (Amsterdam: North-Holland/Elsevier) pp 289–452
[2] Coey J M D 1978 *J. Appl. Phys.* **49** 1646
[3] Taylor R C, McGuire T R, Coey J M D and Gangulee A 1978 *J. Appl. Phys.* **49** 2885
[4] Harris R, Plischke M and Zuckermann M J 1973 *Phys. Rev. Lett.* **31** 160
[5] Sellmyer D J and O'Shea M J 1982 *Recent Progress in Random Magnets* ed D H Ryan (Singapore: World Scientific) pp 71–121
[6] Kaneyoshi T 1984 *Amorphous Magnetism* (Boca Raton, FL: Chemical Rubber Company Press) pp 153–81
[7] Chaudhari P, Cuomo J J and Gambino R J 1973 *IBM J. Res. Dev.* **17** 66

[8] Coey J M D, Chappert J, Rebouillat J P and Wang T S 1976 *Phys. Rev. Lett.* **36** 1061
[9] Rhyne J J, Pickart S J and Alperin H A 1972 *Phys. Rev. Lett.* **29** 1562
[10] Rhyne J J, Schelling J H and Koon N C 1974 *Phys. Rev.* B **10** 4672
[11] Krishnan R and Lassri H 1989 *Solid State Commun.* **69** 803
[12] Teillet J, Lassri H, Krishnan R and Laggoun A 1990 *Hyperfine Interact.* **55** 1083
[13] Krishnan R and Lassri H 1990 *Solid State Commun.* **73** 467
[14] Krishnan R, Lassri H and Teillet J 1991 *J. Magn. Magn. Mater.* **98** 155
[15] Krishnan R, El Marrakchi O and Lassri H 1991 *Solid State Commun.* **77** 567
[16] Krishnan R, Lassri H and Radwánski R J 1992 *Appl. Phys. Lett.* **61** 354
[17] Lassri H and Krishnan R 1992 *J. Magn. Magn. Mater.* **104–107** 157
[18] Krishnan R, El Marrakchi O, Lassri H and Rougier P 1993 *J. Appl. Phys.* **73** 7599
[19] Radwánski R J, Krishnan R, Franse J J M, Lassri H and El Marrakchi O 1993 *Int. J. Mod. Phys.* B **7** 950
[20] Radwánski R J, Franse J J M, Krishnan R and Lassri H 1993 *J. Magn. Magn. Mater.* **119** 221
[21] Krishnan R, Lassri H, Driouch L, Kayzel F E and Franse J J M 1994 *J. Magn. Magn. Mater.* **131** L297
[22] Hassanain N, Lassri H, Krishnan R and Berrada A 1995 *J. Magn. Magn. Mater.* **146** 37
Hassanain N, Lassri H, Krishnan R and Berrada A 1995 *J. Magn. Magn. Mater.* **146** 315
[23] Slimani M, Hamdoun M, Itri A, Lassri H and Krishnan R 1996 *J. Magn. Magn. Mater.* **163** 349
[24] Krishnan R, Driouch L, Lassri H, Dumond Y, Ajan A, Shringi S N and Prasad S 1996 *J. Magn. Magn. Mater.* **163** 353
[25] Driouch L 1995 *Thesis* Rouen University
[26] Laggoun A, Teillet J, Lassri H, Krishnan R and Papaefthymiou G C 1989 *Solid State Commun.* **71** 79
[27] Kubaschewski O 1982 *Iron-Binary Phase Diagrams* (Berlin: Springer) p 15
[28] Ravach G, Teillet J, Fnidiki A, Le Breton J M, Driouch L and Hassanain N 1996 *J. Magn. Magn. Mater.* **157+158** 173
[29] Teillet J and Varret F 1976 *MOSFIT Program* Le Mans University (unpublished)
[30] Varret F 1982 *Proc. Int. Conf. on the Applications of the Mössbauer Effect* (New Delhi: Indian National Science Academy) pp 129–140
[31] Bouchet B 1997 private communication
[32] Bouchet-Fabre B, Kebab A and Dixmier J 1993 *J. Non-Cryst. Solids* **156–158** 161
[33] Bouchet-Fabre B, Kebab A, Dixmier J, Lassri H and Krishnan R 1995 *J. Non-Cryst. Solids* **192–193** 355
[34] Srivastava J K, Bhargava S C, Iyengar P K and Thosar B V 1983 *Advances in Mössbauer Spectroscopy* ed B V Thosar, P K Iyengar, J K Srivastava and S C Bhargava (Amsterdam: Elsevier) ch 1
[35] Greneche J M and Varret F 1982 *J. Physique Lett.* **43** L233
Greneche J M and Varret F 1982 *J. Phys. C: Solid State Phys.* **15** 5333
Greneche J M and Varret F 1985 *Solid State Commun.* **54** 985
[36] Janot C 1983 *Les Amorphes Métalliques* (Aussois: Les Editions de Physique) pp 98–104